

Pressure-tuning structural and electronic transitions in semimetal CoSb

HPSTAR
1224-2021Mingtao Li¹, Deju Zhang², Jia Han³, Yifei Fang⁴, Nana Li¹, Xuqiang Liu¹, Bihan Wang¹, Limin Yan¹,
Fei Chen^{3,*}, Yan-Ling Li^{2,†} and Wenge Yang^{1,‡}¹Center for High Pressure Science and Technology Advanced Research, Shanghai 201203, China²School of Physics and Electronic Engineering, Jiangsu Normal University, Xuzhou 221116, China³Materials Genome Institute, Shanghai University, Shanghai 200444, China⁴Innovation and Integration Center of New Laser Technology, Shanghai Institute of Optics and Fine Mechanics, Chinese Academy of Sciences, Shanghai 201800, China

(Received 27 April 2021; revised 15 July 2021; accepted 16 July 2021; published 13 August 2021)

Recently, theoretical work predicted that the cobalt mono-antimonide (CoSb) with a NiAs-type structure could be stabilized in the form of a monolayer PbO-type FeSe structure on a SrTiO₃ substrate [Ding *et al.*, *Phys. Rev. Lett.* **124**, 027002 (2020)], which may host high-temperature superconductivity comparable with monolayer FeSe [Wang *et al.*, *Chin. Phys. Lett.* **29**, 037402 (2012)]. Motivated to explore the possible pressure-induced superconductivity in bulk CoSb associated with structural instability, utilizing the diamond anvil cell technique, we herein report a comprehensive study of the electrical transport, crystalline structure, and electronic band structure of the bulk CoSb with electrical conductivity, synchrotron x-ray diffraction, and first-principles calculations. No pressure-induced superconductivity is detected down to 2 K with pressure up to 42.0 GPa, but a structural phase transition occurs between 11.7 and 16.2 GPa. Instead, an electronic transition, featured by a carrier-type switch from an electron ($n \rightarrow p$) dominant one at higher pressure, is observed. The n - p switch at room temperature is ascribed to a pressure-induced structural phase transition from hexagonal ($P6_3/mmc$, No. 194) to orthorhombic ($Pnma$, No. 62), which is confirmed by a combination of first-principles calculations and structural refinement. Interestingly, the temperature-driven p - n switch also occurs in the orthorhombic phase at ~ 90 K, emphasizing the tunable multiband structure (with charge neutrality point) of the semimetal CoSb by pressure or temperature. Moreover, the electronic transition is assigned as a semimetal-semimetal transition. The resistivity shows a robust T^3 dependence trend < 30 K for both semimetal phases. At high temperature, all the $\rho(T)$ curves become saturated, as described by the parallel-resistor model. The results support that the s - d interband scattering dominates the conductivity of both the hexagonal and orthorhombic phases under pressure. The superconductivity absence implications are discussed, assuming the electron-phonon interaction in CoSb drives the superconductivity.

DOI: 10.1103/PhysRevB.104.054511

I. INTRODUCTION

The phases of binary 3d transition metal (TM) mono-antimonide TM_{1±x}Sb commonly appear with a defective hexagonal NiAs-type structure, whose composition has a deviation from the ideal 1:1 stoichiometry [1,2]. Among TM_{1±x}Sb mono-antimonides, the Ni-Sb and Co-Sb phases exceptionally extend to a considerable range of homogeneity on both sides of the stoichiometric 1:1 composition [1,2]. Hence, there are two defective sites, either a subtractive type due to the vacant TM sites or an additive type to insert additional TM atoms on the interstitial sites [3]. At ambient conditions, Co_{1±x}Sb is predicted and demonstrated to be a paramagnetic metal [4–6].

Recently, the Co-Sb binary compounds have attracted increasing interest due to their high-performance thermoelectric

properties in CoSb₃ [7,8], and the potential high-transition temperature (T_c) superconductivity in monolayer CoSb [9]. To date, only a few cobalt-based compounds have been demonstrated to be superconducting, including the CoSi₂ ($T_c \approx 1.4$ K) [10], intermetallic UCoGe ($T_c \approx 0.8$ K) [11], CeCoIn₅ ($T_c \approx 2.3$ K) [12], layered Na_xCoO₂ · yH₂O ($T_c \approx 5$ K) [13], and layered LaCo₂B₂ with Y or Fe doping ($T_c \approx 4$ K) [14]. Thus, discovering more superconducting cobalt-based compounds is a challenge. Theoretically, Hu *et al.* [15] propose that high- T_c superconductivity exists in Co-based compounds formed by cation-anion trigonal bipyramidal complexes with a d^7 filling configuration on the cation ions. In monolayer compounds, Ding *et al.* [9] predicted that the most stable structure for CoSb is a PbO type, which is an analog of the high- T_c FeSe superconductor. Further, theoretical calculations on the band structure and electron-phonon coupling of monolayer CoSb show that it can host high- T_c superconductivity like monolayer FeSe [16]. If this can be experimentally realized, it would open a high- T_c family beyond the cuprates and iron-based superconductors. Interestingly, a weak superconducting signal at ~ 14 K was lately discovered

*Corresponding author: chf001@t.shu.edu.cn

†Corresponding author: ylli@jsnu.edu.cn

‡Corresponding author: yangwg@hpstar.ac.cn

in the MBE-grown monolayer CoSb with an orthorhombic structure [17].

Pressure is an effective and clean tool for tuning the structural and physical properties in various matters [18,19]. The electron-phonon interaction (EPI) may be particularly enhanced due to structural instability appearing at the boundary of the pressure-induced structural phase transition (SPT). On the other hand, the crystallographic lattice symmetry and coordination number may concomitantly change after the completion of the SPT, leading to the strong modification of the band structure and chemical and physical properties. For instance, pressure has been successfully adopted to induce superconductivity in topological materials [20,21], a topological phase [22,23], and improve thermoelectric performance [24]. As mentioned above, the bulk NiAs-type CoSb phase could transform to a stable FeSe-like structure in monolayer form [9], which is predicted to host high- T_c superconductivity. This motivated us to conduct a high-pressure investigation of the electrical transport and structure in bulk CoSb to explore if pressure-induced structural instability drives the superconductivity.

II. EXPERIMENTAL METHODS

A. Sample synthesis

The polycrystalline CoSb sample was synthesized via the solid-state reaction method. The cobalt powder and antimony granules were put into an alumina crucible in a stoichiometric ratio of 1:1 and then sealed in an evacuated quartz tube. The mixtures were heated at 1023 K for 12 h and further annealed at 1373 K for 5 d. After that, the CoSb ingot was obtained by furnace cooling. Single crystals of CoSb were grown via a chemical vapor transport method using iodine as a transport agent (15 mg/cm³) and the polycrystalline CoSb powder. More details can be found in a previous report [5]. The powder and compositions of the single-crystal samples were determined by energy-dispersive x-ray spectroscopy (EDS) using an Oxford X-MAX^N 20 spectrometer. The morphology of the powder sample was obtained on a FEI Versa 3D scanning electron microscope.

B. Electrical transport measurements under pressure

Ambient and high-pressure electrical transport measurements were performed using the standard four-probe method under van der Pauw configuration in a commercial DynaCool physical property measurement system (PPMS, QD) [25]. Specifically, the electrical transport measurement <2 K was carried out on the adiabatic demagnetization regulator option attached to the PPMS. A nonmagnetic BeCu diamond anvil cell (DAC) was used to generate high-pressure conditions. A pair of diamonds beveled from 400 μm to a culet of 250 μm was used. A nonmagnetic BeCu alloy gasket was used with an initial thickness of 250 μm . The pre-indented hole was covered by cubic boron nitride (C-BN) as an insulating layer (thickness ~ 37 μm). Subsequently, a hole with a 100 μm diameter was laser drilled as the sample chamber, where the ground fine CoSb powder was loaded. A small ruby ball was put on the powder sample for pressure calibration. Four pieces of platinum foil were utilized as the contacts.

C. Synchrotron x-ray diffraction (XRD) structure measurements under pressure

The high-pressure synchrotron angle-dispersive XRD of the CoSb powder was measured at the 15U1 station (x-ray wavelength $\lambda = 0.6199$ \AA), Shanghai synchrotron radiation facility (SSRF), China. A symmetric Mao-Bell DAC was used to generate high-pressure conditions. Mineral oil was used as the pressure-transmitting medium. The raw two-dimensional (2D) XRD images were integrated into one-dimensional intensity vs 2θ angles using the DIPTAS program [26]. The distance between the sample and detector and the detector tilting angles were calibrated using standard CeO₂ powder diffraction. The XRD patterns were further analyzed by Rietveld refinement using the GSAS program package with the user interface EXPGUI [27,28]. The actual pressure in this paper was determined from the standard ruby fluorescence [29].

D. Theoretical calculations

First-principles calculations were performed with the Vienna *ab initio* Simulation Package (VASP) based on the density functional theory [30,31]. Combined with VASP [30,31], the most stable structure of CoSb at high pressure was searched via the evolutionary algorithm USPEX code [32,33]. The calculated results were obtained by employing the exchange-correlation function of Perdew-Burke-Ernzerhof [34], and the projected augmented wave method [35,36]. The spin-orbit coupling (SOC) was considered in the electronic structure calculations. In detail, a basis set cutoff of 400 eV was adopted for both structural relaxations and electronic structure calculations. The $3p^63d^74s^2$ and $5s^25p^3$ configurations were treated as valence electrons for Co and Sb atoms, respectively. For the structural search, a coarse k -point grid was used firstly before using a spacing $2\pi \times 0.018$ \AA^{-1} for the most interesting structures. The k -grids in Brillouin zone were $9 \times 9 \times 7$ for the $P6_3/mmc$ phase at ambient pressure and $6 \times 8 \times 6$ for the $Pnma$ phase at high pressure in the structural relaxations and electronic structure calculations, respectively.

III. RESULTS AND DISCUSSIONS

A. Sample characterization and structural evolution at high pressure

At ambient pressure, cobalt mono-antimonide CoSb crystallizes in a NiAs-type structure (hexagonal, space group $P6_3/mmc$, No. 194, $Z = 2$). Figure 1 depicts the stacking sequence of face-shared octahedral Co-Sb. The distinct features of the crystal structure viewed along different crystallographic axes are displayed at the right side of the main panel of Fig. 1(a). Figure 1(b) shows the XRD pattern of the pristine CoSb sample at ambient conditions. No additional peaks are observed, indicating the phase purity of the experimental powder sample. Further Rietveld refinement yields the lattice parameters $a = b = 3.9006(8)$ \AA , $c = 5.2158(1)$ \AA , which are consistent with previous reports [4,5,37]. This yields a lattice ratio $c/a = 1.337$, which indicates the subtractive-type deviation from the ideal NiAs-type stoichiometry 1:1 [2]. Using the energy-dispersive spectroscopy (EDS), the compositions of powder and single-crystal samples were determined to be

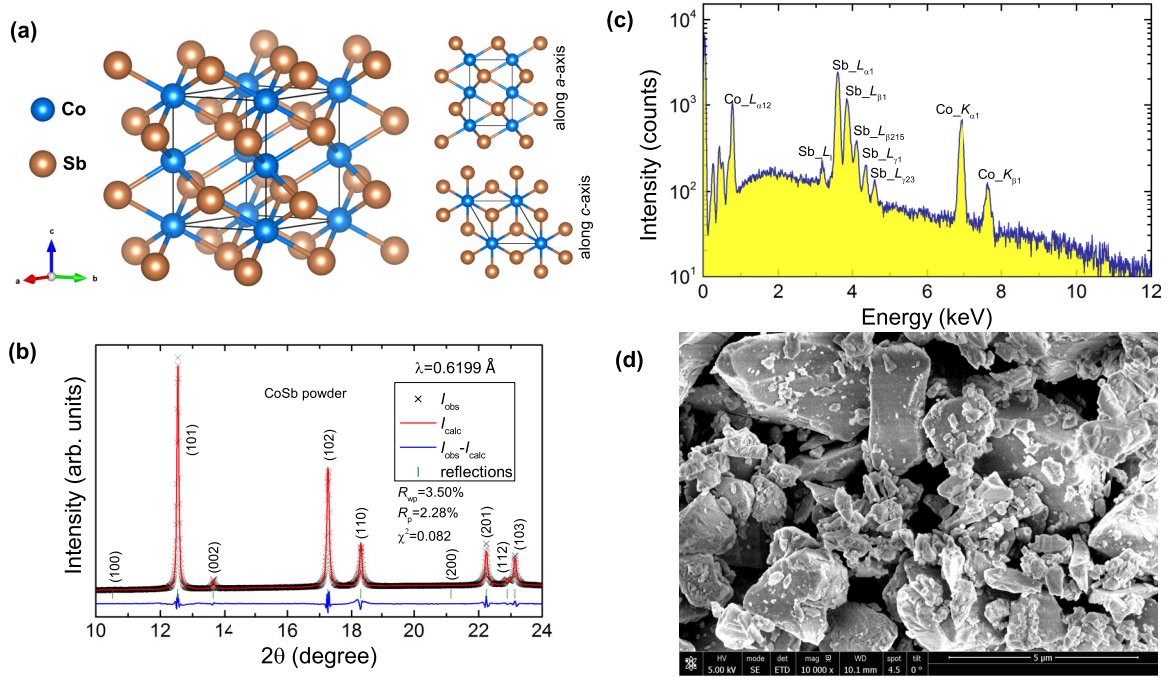


FIG. 1. (a) Crystal structure of CoSb viewed along different directions. (b) Refined synchrotron x-ray diffraction (XRD) patterns of pristine CoSb powder at ambient pressure. (c) Energy-dispersive spectroscopy (EDS) of the CoSb powder and its surface morphology. (d) Scanning electron microscopy of the pristine CoSb sample.

$\text{Co}_{0.99(4)}\text{Sb}$ and $\text{Co}_{1.01(1)}\text{Sb}$. A typical EDS profile is displayed in Fig. 1(c). The morphology of the pristine CoSb sample is shown in Fig. 1(d), with a grain size of $\sim 1\text{--}5 \mu\text{m}$. The c/a ratio of CoSb is slightly smaller than that of NiAs ($c/a = 1.39$) [4], which is also metallic. According to Pearson's criterion [6], a small c/a ratio can cause the mutual TM atoms to approach sufficiently close to form a d band instead of the discrete d states, resulting in the metallic behavior. Here, $\text{Co}_{1\pm x}\text{Sb}$ is demonstrated to be a paramagnetic metal [4–6], in good agreement with Pearson's scenario.

We carried out synchrotron XRD measurements of the CoSb powder to explore the structural instability induced by pressure. Selected XRD patterns are presented in Fig. 2(a). Distinct reflections emerge >11.7 GPa under compression, signifying the occurrence of pressure-induced SPT. The structure is determined to be orthorhombic ($Pnma$, No. 62), as discussed later in Sec. III C.

The pressure-dependent lattice parameters are plotted in Fig. 2(b). The intermediate pressure region, where the hexagonal and orthorhombic phases coexist, ranges from 11.7 to 36.1 GPa over an interval of ~ 24 GPa. The phase coexistence can also be seen in the three-dimensional (3D) plot of selected XRD patterns in Fig. S1(a) in the Supplemental Material [38], and the Rietveld refinement profile at 26.4 GPa was plotted in Fig. S1(b) in the Supplemental Material [38]. Also, the refined results for ambient pressure and 40.2 GPa phases were summarized in Table S1 in the Supplemental Material [38]. The SPT of hexagonal \rightarrow orthorhombic is predicted to complete at ~ 32 GPa, in good agreement with our experimental observation. Also, a volume collapse of 4.64% at 32.0 GPa implies a first-order SPT. To compare the compression behavior, we fitted the formula unit cell volume vs pressure $\frac{V}{Z}(P)$ using the third-order Birch-Murnaghan equation of state

(BM-EoS) [39] $P = 3K_0 f_E (1 + 2f_E)^{5/2} \cdot [1 + \frac{3}{2}(K'_0 - 4)f_E]$, where $f_E = [(V_0/V)^{2/3} - 1]/2$ is the Eulerian strain, K_0 is the bulk modulus, K'_0 is the pressure derivative of K_0 , and V_0 is the volume at ambient pressure. The best fitting yields $K_0^h = 161.7(17.3)$ GPa, $K_0^{h'} = 3.5(1.2)$ and $V_0^h = 33.3(1) \text{ \AA}^3$ for the hexagonal phase and $K_0^o = 195.2(82.8)$, $K_0^{o'} = 2.0(1.8)$, and $V_0^o = 31.6(1.0) \text{ \AA}^3$ for the orthorhombic phase.

B. Electrical transport under pressure

1. Robust $\rho(T) \approx T^3$ relationship at low temperature

Figure 3(a) shows the temperature dependence of resistivity $\rho(T)$ measured on a CoSb single crystal at ambient pressure, which behaves metallically in the whole temperature region. No superconductivity was detected down to 0.165 K, as seen in the lower panel insets. At low temperature ($T < 50$ K), the $\rho(T)$ follows $\rho(T) = \rho_0 + AT^{n'}$ well with $n' = 2.70(8)$, which approaches the low-temperature limit $\rho(T) \approx T^3$ for the interband s - d scattering of transition metals [40]. This indicates a weak contribution to conductivity from the electron-electron scattering at low temperature. As shown in Fig. 3(b), the positive Hall coefficient R_H indicates the dominant contributions to conduction are from hole carriers in the range of 2–350 K. Furthermore, the deduced carrier density is of $3.0 \times 10^{22} \text{ cm}^{-3}$ at 2 K [see Fig. 3(c)] and shows an increasing trend with a weak temperature dependence. The results are consistent with previous work on single-crystal CoSb reported by Xian *et al.* [5]. We also measured the Hall effect on a polycrystalline piece (see Fig. S2 in the Supplemental Material [38]), which also shows the positive slope of Hall resistance vs magnetic field, supporting the hole-type carriers.

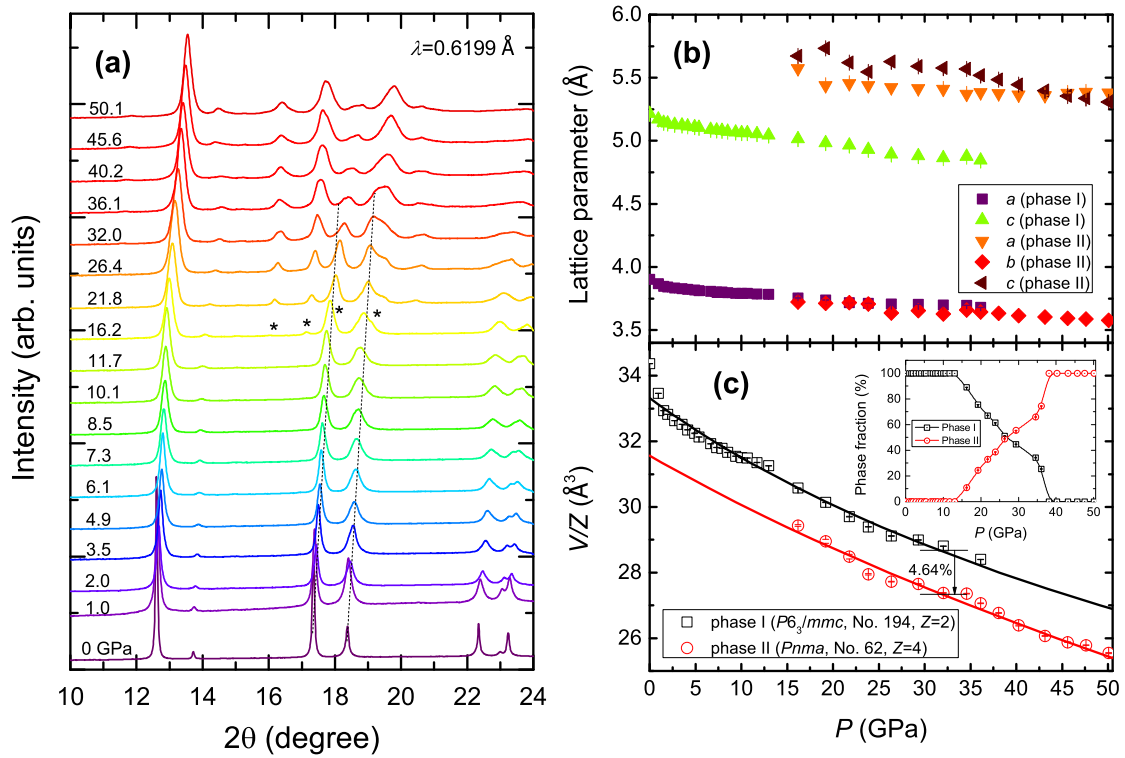


FIG. 2. (a) Selected synchrotron x-ray diffraction (XRD) patterns for CoSb powder. The dashed lines guide the evolution of reflections from hexagonal phases. The asterisks indicate the emergence of new reflections from orthorhombic phases. (b) Lattice parameters and (c) formula unit cell volume as a function of pressure. Inset of (c) shows the phase fraction vs pressure.

To explore the electrical transport properties of bulk CoSb at high pressure, we measured its temperature dependence of resistivity $\rho(T)$ up to 42.0 GPa, as shown in Fig. 4(a). On the one hand, all the $\rho(T)$ curves display metallic behavior,

consistent with previous reports and our results at ambient pressure [4–6]. On the other hand, they tend to saturate at high temperature and become more and more prominent at higher pressures. No superconducting transition is observed

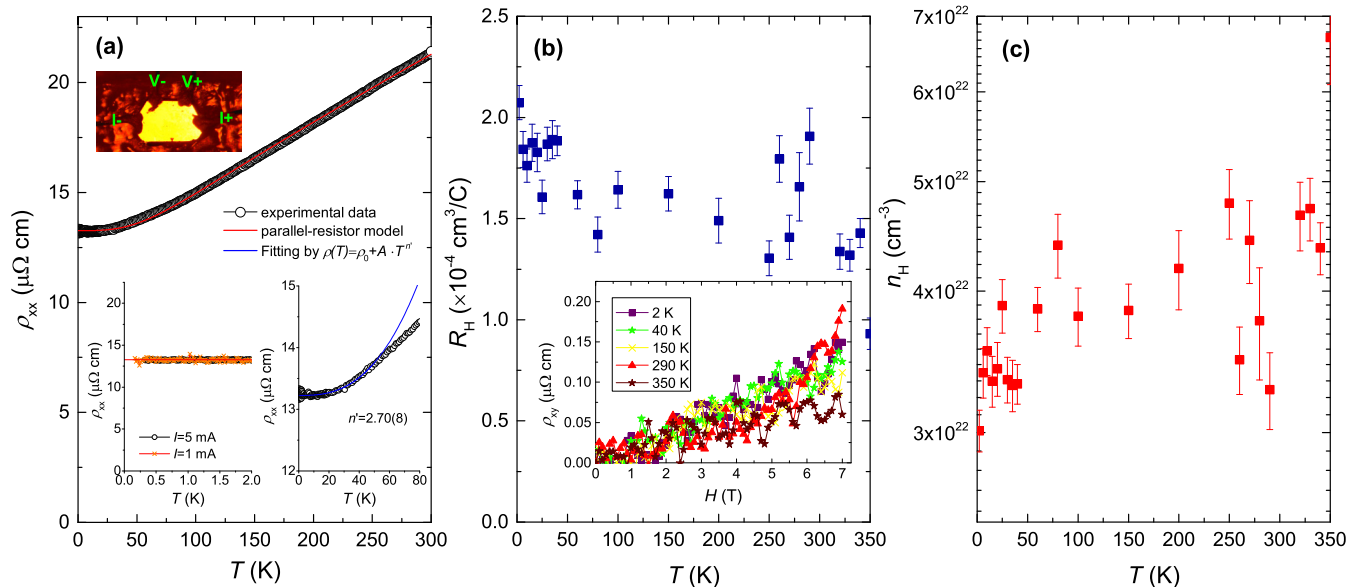


FIG. 3. (a) Temperature-dependent resistivity of single-crystal CoSb with a $\sim 0.72 \times 0.47 \times 0.10 \text{ mm}^3$ size at ambient pressure. The upper-left inset depicts single-crystal morphology with a shining surface and four conducting leads arrangement. The lower panels show the magnified region of $\rho(T)$ in the low-temperature regions of 0.165–2 K and 0.165–80 K. Solid red and blue lines are the fitting curves by parallel-resistor model and $\rho(T) = \rho_0 + AT^n$. (b) Temperature dependence of Hall coefficient. Inset shows the Hall resistance vs magnetic field at selected temperatures. (c) Temperature dependence of Hall carrier density.

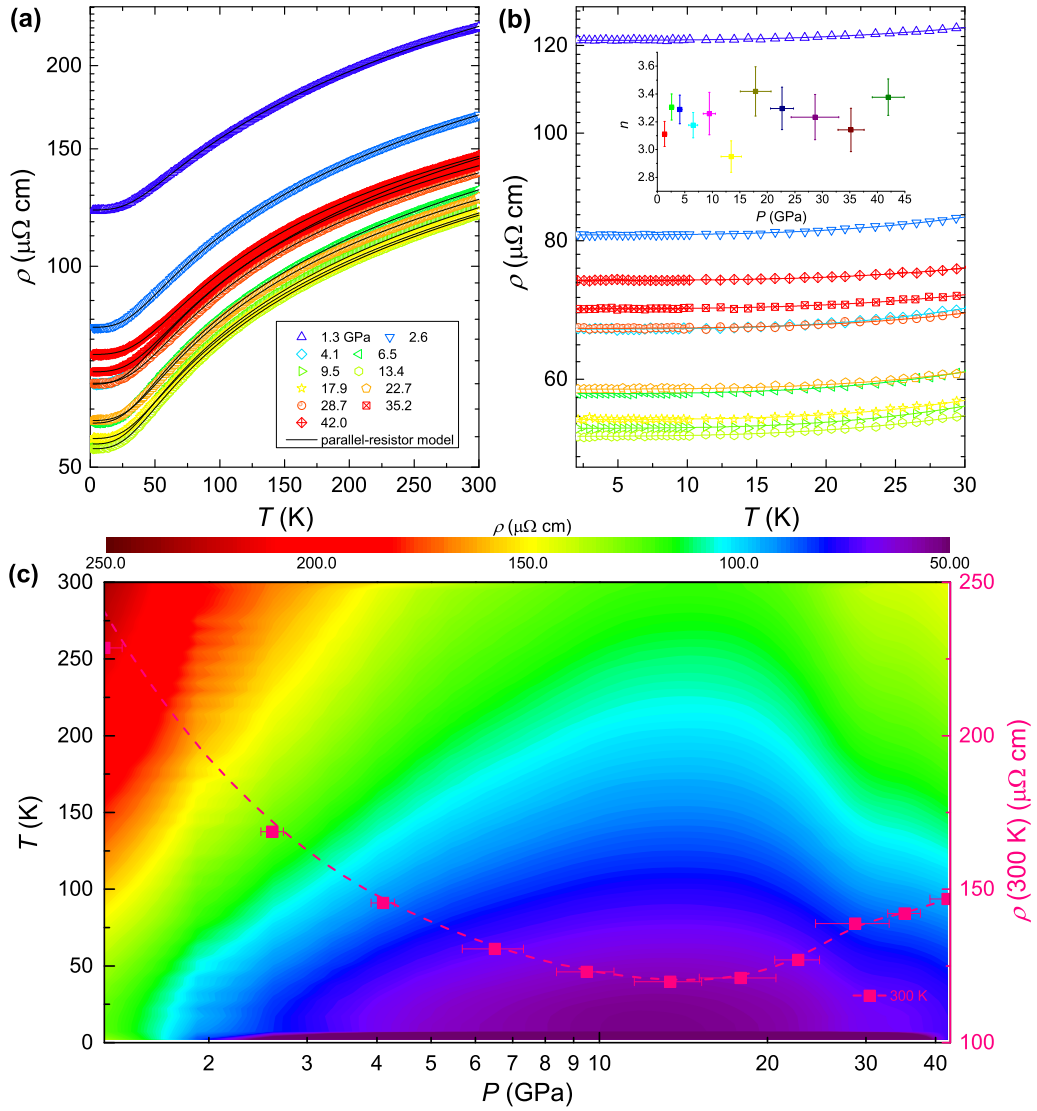


FIG. 4. (a) Temperature dependence of resistivity for CoSb powder at different pressures. The solid lines are the parallel-resistor model fitting curves. (b) Temperature dependence of resistivity <30 K at different pressures. Solid lines are the fitting curves by $\rho(T) = \rho_0 + AT^{n'}$. Inset shows the evolution of the n' value with pressure. (c) Contour plot of the resistivity vs temperature with a function of pressure. The color distribution represents the resistivity value. The room temperature (300 K) $\rho(P)$ from 1.3 to 40 GPa is also displayed as solid squares.

down to 2 K for pressurized CoSb <42.0 GPa. The resistivity saturation and its pressure dependence have also been reported in other semimetals like TaAs₂ [41]. At ambient pressure, it is widely observed in intermetallic TM, too, such as the A-15 compounds, including V₃Si [42] and Nb₃Sn [43,44] and many other materials [45,46]. The CoSb resistivity saturation will be discussed quantitatively later. When assuming the conduction electrons are only scattered by longitudinal acoustic phonons and the contribution of electron-electron scattering is ignored, the $\rho(T)$ data can be described by a modified Bloch-Grüneisen model [40,42,47–49]:

$$\rho_{\text{BG}}(T) = \rho_0 + \rho_{sd} \left(\frac{T}{\Theta_R} \right)^3 \int_0^{\Theta_R/T} \frac{x^3 dx}{(1 - e^{-x})(e^x - 1)} + \rho_{ss} \left(\frac{T}{\Theta_R} \right)^5 \int_0^{\Theta_R/T} \frac{x^5 dx}{(1 - e^{-x})(e^x - 1)}, \quad (1)$$

where Θ_R is the resistivity-determined Debye temperature, ρ_0 is residual resistivity due to impurity scattering, the second term is ascribed to the interband s - d scattering of transition metals [40], and the intraband s - s scattering for the third term. As shown in Fig. 4(a), we fitted the $\rho(T)$ curves by the parallel-resistor model [45,50,51] to understand the resistivity saturation behavior:

$$\frac{1}{\rho} = \frac{1}{\rho_{\text{sat}}} + \frac{1}{\rho_{\text{BG}}}. \quad (2)$$

Before fitting into Eq. (1), the dominant term at low temperature will be examined. As shown in Fig. 4(b), the fittings of the low-temperature $\rho(T)$ curves by $\rho(T) = \rho_0 + AT^{n'}$ (where A is a constant and the n' variable exponent with $n' = 2$ represents the electron-electron scattering) show that all $\rho(T)$ curves dominantly obey the $\rho(T) \approx T^3$ for all pressures. For this reason, only the ρ_{sd} term is incorporated in the fitting

TABLE I. Fitting parameters for pressurized CoSb by parallel-resistor model.

P (GPa)	ρ_0 ($\mu\Omega$ cm)	ρ_{sd} ($\mu\Omega$ cm)	ρ_{sat} ($\mu\Omega$ cm)	Θ_R (K)
Fitted by Eq. (2)				
1.3(1)	148.8(4)	343.3(5.3)	661.6(8.0)	248.5(2.0)
2.6(1)	99.9(1)	281.8(2.2)	428.4(2.0)	231.1(1.0)
4.1(2)	81.8(1)	242.0(1.2)	359.0(1.0)	219.3(6)
6.5(8)	71.5(0)	222.5(1.0)	313.0(7)	215.6(6)
9.5(1.1)	66.7(1)	213.8(1.1)	288.6(8)	215.0(7)
13.4(1.8)	65.9(1)	214.4(1.3)	278.0(9)	219.6(8)
17.9(2.8)	68.8(1)	227.6(2.0)	278.8(1.3)	233.7(1.2)
22.7(2.1)	74.6(1)	254.4(2.2)	276.9(1.2)	237.1(1.2)
28.7(4.3)	85.9(1)	310.8(2.7)	299.8(1.3)	265.2(1.2)
35.2(2.4)	91.2(1)	342.5(2.2)	291.6(9)	270.3(9)
42.0(2.9)	97.5(1)	373.0(2.9)	303.8(1.2)	291.9(1.1)

using Eq. (2). Also, the statistics are better than those obtained using the ρ_{ss} term. The fitting results are summarized in Table I. This indicates that the interband s - d scattering dominates the normal state conduction in CoSb.

The Co atoms predominantly contribute to the interband s - d scattering due to the unfilled $3d$ orbital [40,44]. It should be pointed out that many pure transition metals and rare-earth metals show $\rho \approx T^2$ at low temperature [52], rather than the compliance of $\rho \approx T^5$ expected from the Bloch-Grüneisen theory in pure monovalent metals [47,53]. In comparison, the robust $\rho(T) \approx T^3$ at low temperature is also observed in TaAs₂ semimetal up to 36.6 GPa [41], which shows no superconducting transition down to 2 K. Note that the best fit of $\rho(T)$ using the ρ_{sd} term was also reported in the A-15 superconductor V₃Si with strong electron-phonon coupling [42], but the T_c decreases when the exponent n' changes from two to higher values. This emphasizes the important role of the $\rho(T) \approx T^2$ part in optimizing the T_c therein. The

appearance of resistivity saturation is treated as a signature of the strong EPI and weak electron-electron interaction (EEI) [54,55]. Strong EPI alone does not guarantee a superconducting transition at low temperature, so it seems that the moderate EEI can optimize the T_c , as demonstrated in iron-based superconductors [56].

We plotted the contour of the resistivity vs temperature as a function of pressure to examine the pressure effect on the normal state properties, as shown in Fig. 4(c). For clarity, we also extracted the pressure-dependent resistivity at 300 K. Interestingly, the resistivity firstly decreases with increasing pressure before reaching a minimum at ~ 13.4 GPa at ambient temperature, which also exists at other constant temperatures. Above 13.4 GPa, the resistivity starts to anomalously increase up to 42.0 GPa. This is unusual since pressure commonly causes bandwidth broadening for a normal metal to increase the carrier density, which further results in a decrease of resistivity.

2. Carrier-type p - n switch

The pressure dependence of the Hall effect was analyzed at 2, 20, and 300 K to understand this abnormally electrical transport property. The Hall resistances vs magnetic field $R_{xy}(H)$ at 300 K are displayed in Fig. 5(a). Below 9.5 GPa, the $R_{xy}(H)$ shows linear field dependence with negative slopes, indicative of dominant electron-type (n -type) carriers, in contrast to the dominant hole-type carriers at ambient pressure. In the two-band model, the Hall coefficient R_H can be written as $R_H = \frac{1}{e} \frac{n_h \mu_h^2 - n_e \mu_e^2}{(n_h \mu_h + n_e \mu_e)^2}$ in a low field limit [57]. Thus, R_H will change sign as the tuning of magnitude of $n_h(n_e)$ and $\mu_h(\mu_e)$ by either chemical doping, temperature, or external pressure. Although the transport data is difficult to collect at low pressure using a powder sample in a DAC, we conjecture that the pressure could modify the band structure topology of CoSb to change the relative den-

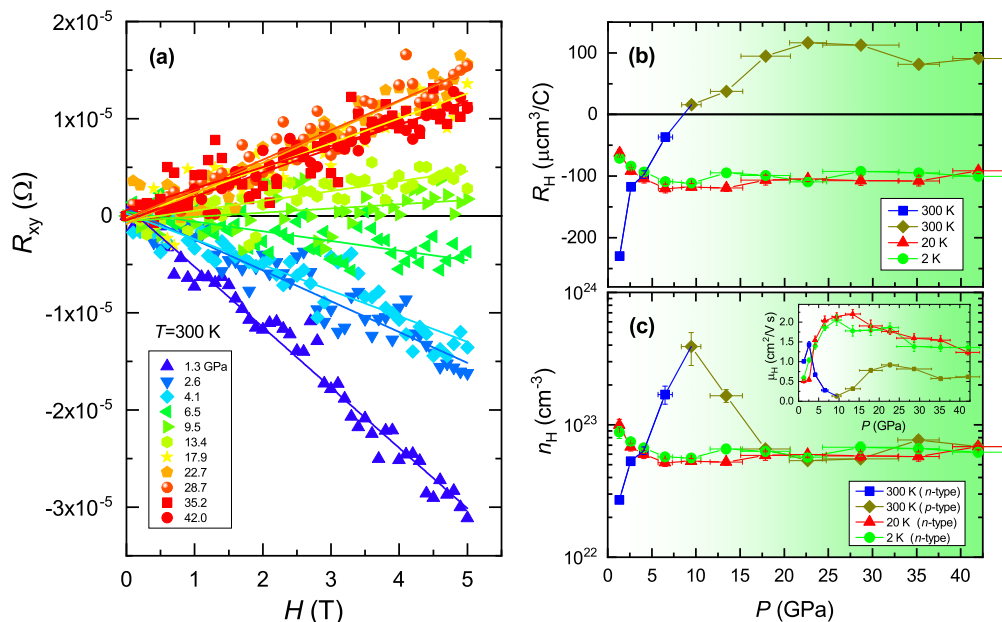


FIG. 5. (a) Field dependence of Hall resistance at various pressures at 300 K. Pressure dependence of (b) Hall coefficient and (c) Hall carrier density at 2, 20, and 300 K. Inset of (c) shows the Hall mobility as a function of pressure.

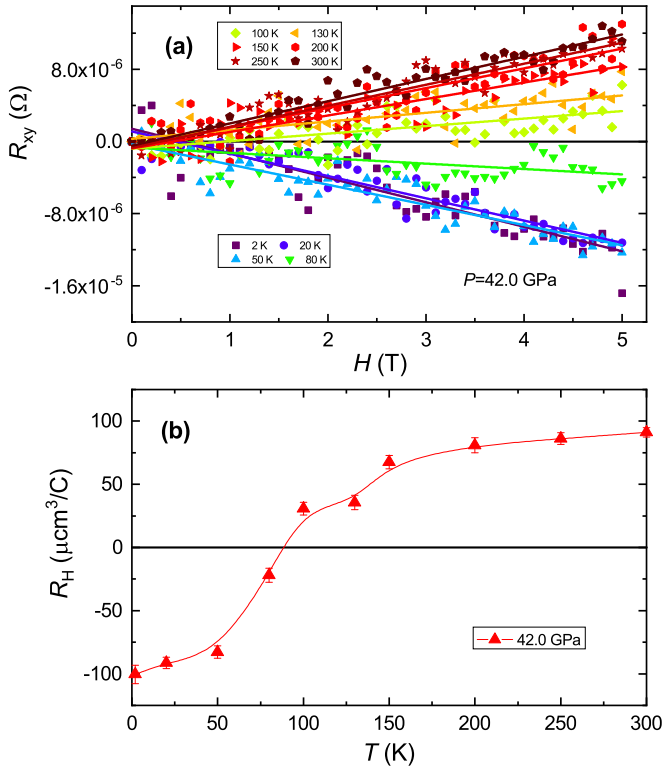


FIG. 6. (a) Field dependence of Hall resistance at different temperatures. (b) The Hall coefficient as a function of temperature at 42.0 GPa.

sity and scattering rate of hole and electron, which induces a carrier type switch at low pressure ($P < 1.3$ GPa). After releasing the pressure to 1.40 and 0.55 GPa, the hole-type carriers become dominant again at 300 K (see Fig. S4 in the Supplemental Material [38]), implying its subtle electronic response to the application of mild pressure. In addition, the consistent evidence of supporting its electronic sensitivity to mild pressure comes from the fast compression rate of unit cell volume < 2 GPa [see Fig. 2(c)]. The observation of pressure-induced carrier-type change in Hall coefficient measurement < 2 GPa implies the initial fast volume compression has an electronic origin. Nevertheless, the slope of $R_{xy}(H)$ becomes positive (hole carriers, p type) > 9.5 GPa, signaling a n - p switch and pressure-induced charge neutrality point (CNP) at 300 K. Note that the symmetrized $R_{xy}(H)$ was obtained by the difference of the Hall resistance at positive and negative fields to eliminate the longitudinal contribution, i.e., $R_{xy}(H) = [R_{xy}(+H) - R_{xy}(-H)]/2$. The Hall mobility μ_H was further determined by $\mu_H = (d/\rho)R_{xy}/H$ [25], where d is the sample thickness. We plotted the Hall coefficient R_H , carrier density n_H , and μ_H as a function of pressure in Figs. 5(b) and 5(c). Clearly, a temperature-driven p - n switch also exists > 9.5 GPa, as shown in Fig. 5(b).

We measured the temperature-dependent $R_{xy}(H)$ at 42.0 GPa to determine the temperature-driven CNP, as shown in Fig. 6(a). More Hall data at 17.9 and 28.7 GPa can be found in Fig. S3 in the Supplemental Material [38]. Figure 6(b) plots the corresponding $R_H(T)$ curves, unveiling that the CNP sets in at ~ 90 K. The n_H increases < 9.5 GPa at 300 K, which causes the fast decrease of the resistivity. However, the n_H

starts to decline > 9.5 GPa, which may explain the unusual increase of resistivity according to the simple Drude law $\rho = m^*/ne^2\tau$, where m^* is carrier effective mass, n carrier density, e electron charge, and τ the carrier scattering rate. Above 17.9 GPa, a negligible temperature and pressure-dependent n_H is observed. The small values of the μ_H and n_H (in an order of 10^{22} cm $^{-3}$) for the CoSb at ambient and high pressure indicates it is more like a semimetal.

3. Debye temperature Θ_R and mean free path l

Establishing the phase diagram of the $R_H(T, P)$, we now return to discuss the saturation behavior of pressurized CoSb more quantitatively. When the carrier mean free path l approaches the interatomic distance a but will not become much smaller, reaching the so-called Ioffe-Regel condition $l \gtrsim a$, the resistivity in an ordinary metal tends to attain a saturation value, which for a cubic metal is given by [45,51,58]

$$\rho_{\text{sat}} = \frac{1.29 \times 10^{18}}{n^{2/3}a} (\mu\Omega \text{ cm}), \quad (3)$$

where n is the carrier density in units per cubic centimeter, and a is the lattice parameter in angstroms. Assuming a spherical Fermi surface with the Fermi wave number $k_F = (3\pi^2n)^{1/3}$, the mean free path can be rewritten as

$$l = 10^{14} \frac{\hbar(3\pi^2)^{1/3}}{n^{2/3}\rho_0e^2} (\text{\AA}). \quad (4)$$

Combined with Eqs. (3) and (4), one obtains that

$$l = \frac{[\hbar(3\pi^2)^{1/3}a\rho_{\text{sat}}]}{(1.29 \times 10^4\rho_0e^2)} = l_0a. \quad (5)$$

In Eq. (5), l_0 is dimensionless and only proportional to the ratio ρ_{sat}/ρ_0 , where ρ_0 is in units of microhm centimeters. Equation (5) enables us to evaluate the magnitude of the l even though the carrier density is somehow unknown for a resistivity-saturated material. We calculated the l and l_0 values vs pressure using the previously obtained Hall carrier density and fitting data, as shown in Table I.

First, we focus on the resistivity determined Debye temperature Θ_R as a function of pressure, as shown in Fig. 7(a). It is well known that the characteristic Debye temperature characterizes the cutoff frequency for the collective lattice vibrations of a solid below it. At Debye temperature, the phonon frequency wavelength is shown to be comparable with the lattice parameter [59]. Consequently, the pressure-induced anomaly of Θ_R could be an effective indicator of the occurrence of a structural anomaly, e.g., SPT. If there is no pressure-induced SPT, the evolution of $\Theta_R(P)$ will be monotonous since the lattice is to be compressed by external pressure. Unexpectedly, CoSb has a minimum at ~ 9.5 GPa [as shown in Fig. 7(a)], which indicates the appearance of a SPT.

With increasing pressure, the resistivity saturation becomes more and more prominent for CoSb. To understand its origin, we plotted the pressure dependence of l_0 and l in the inset of Fig. 7(a) and the main panel of Fig. 7(b), in which the ρ_{sat}/ρ_0 ratio and lattice parameters are also included for comparison. It turns out that the calculated l based on the simple Drude law is comparable with the experimental lattice parameters. However, the estimated l is 99.4 \AA for single-crystal CoSb,

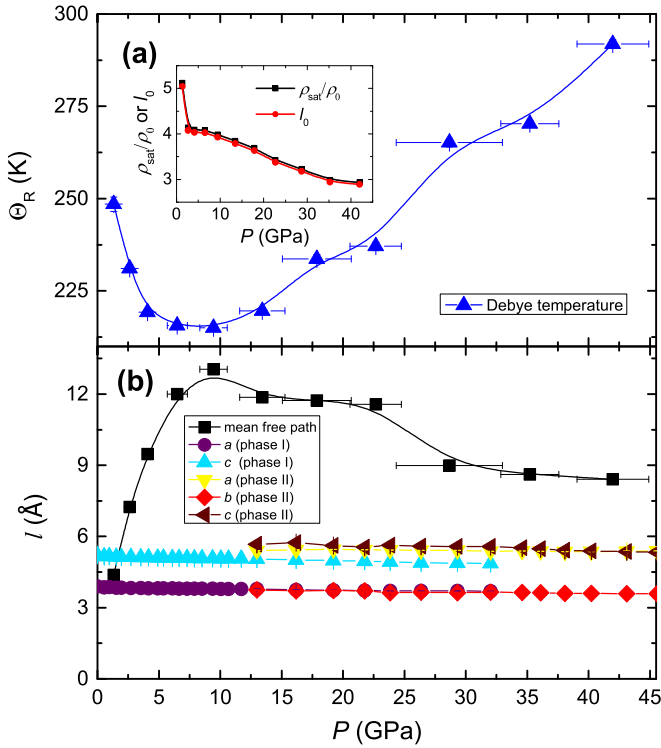


FIG. 7. (a) Pressure dependence of resistive Debye temperature for CoSb. (b) Carrier mean free path as a function of pressure, including lattice parameters for comparison.

which is much larger than the interatomic distances. This may lead to almost linear behavior instead of resistivity saturation in $\rho(T)$ at high temperature. Also, the l_0 obtained by the ρ_{sat}/ρ_0 ratio from the parallel-resistor model fittings supports that the l values have several lattice spaces for pressurized CoSb. At high pressure, the decrease of l_0 with loading pressure could self-consistently interpret the pressure-enhanced resistivity saturation at high temperature because the saturation is unexpected in the limit of $l \gg a$.

C. Band structure calculations

Combined with VASP [30,31], the most stable structure of CoSb at high pressure was searched by the evolutionary algorithm [32,33]. The results show that the orthorhombic structure ($Pnma$, No. 62) is energetically favorable >32 GPa. This structure hosts a distorted Co-Sb octahedral, as depicted in Fig. 8(a). The stability and reliability of the orthorhombic phase are consistently supported by the theoretical prediction on the enthalpy, phonon dispersion, and good Rietveld refinements, as shown in Figs. 8(b)–8(d). Figure 8(b) shows that the pressure dependence of the enthalpy ΔH demonstrates the SPT boundary occurs at 32 GPa, reasonably close to the experimental pressure 36.1 GPa, where the SPT from the hexagonal-to-orthorhombic phase almost completes. The phonon dispersion was further calculated at 33 GPa (just above the SPT boundary). Near the Brillouin zone center (G point), no appearance of imaginary frequency for both the acoustic and optical branches supports that the $Pnma$ phase is thermodynamically stable.

To compare the differences in electronic structure for the hexagonal and orthorhombic phases, we calculated the band structure for the two phases in CoSb. Due to the composite of two heavy ions in CoSb, the SOC might play an important role in controlling its structure and physical property. For this reason, the SOC is included in our band structure calculations. At ambient pressure, bulk CoSb is predicted to be a topological crystalline insulator with Z_{12} invariant when counting the effect of SOC [60]. As seen in Figs. 9(a) and 9(b), it is apparent that there are $3d$ orbitals from Co atom-dominated multibands crossing the Fermi energy (E_F), supporting the multiband feature observed in the electrical transport measurements, i.e., the type switch of the carriers. After the pressure-induced SPT, the calculations also show that the Fermi surface changes significantly, as seen in Figs. 9(c) and 9(d) for hexagonal CoSb at ambient pressure, and Figs. 9(e) and 9(f) for orthorhombic CoSb at 33 GPa. The Fermi surfaces have eight components with complex shapes for both phases. For instance, there are two hourglasslike Fermi surfaces in hexagonal CoSb around the Brillouin zone center. Nevertheless, in the orthorhombic phase, two bowllike Fermi surfaces form up and down to the zone center. This provides solid evidence of the occurrence of an electronic topological transition (ETT) induced by a SPT in CoSb. Moreover, the band structure supports that both phases are more like a semimetal. As seen in Fig. 4(c), the resistivity starts to show an abnormal increase at ~ 13.4 GPa. Concurrently, the Hall coefficient appears a sign change >9.5 GPa, supporting the resistivity anomaly is associated with an ETT triggered by a SPT. The pressure-induced sign change in Hall coefficient was also observed in other semimetals like NiTe_2 [61], which is attributed to the occurrence of Lifshitz transition without a SPT. Our result indicates that the Hall anomaly experimentally characterized by the n - p switch at ~ 9.5 GPa originates from the hexagonal \rightarrow orthorhombic SPT-induced ETT because the orthorhombic phase is ready to set in at the same pressure.

As discussed before, the s - d interband scattering is suggested to account for the conduction in both phases. To gain more insight from the theoretical calculations, we plotted the partial density of states in the right panels of Figs. 9(a) and 9(b). First, the total density of states (DOS) for CoSb at ambient pressure and 33 GPa is 1.15 and 0.90 states/spin eV formula unit cell. This is qualitatively consistent with the Hall carrier density vs pressure at low temperature, which shows that the n_H value of hexagonal CoSb is slightly higher than that of the orthorhombic phase. Secondly, we note that the contribution of the s orbital of the Co(Sb) atoms increased while the contribution by the d orbital of the Co atoms decreased at 33 GPa. Benefitting from the synergetic balance between the s orbital of the Co(Sb) atoms and the d orbital of the Co atoms, this could qualitatively explain the robust ρ_{sd} term contributed from the s - d interband scattering at high pressures.

D. Discussions and implications on absence of superconductivity

Besides the EPI, the EEI is concomitantly one of the key parameters to tune intriguing quantum states like superconductivity for conventional and unconventional superconducting families [56,62]. From the electrical transport

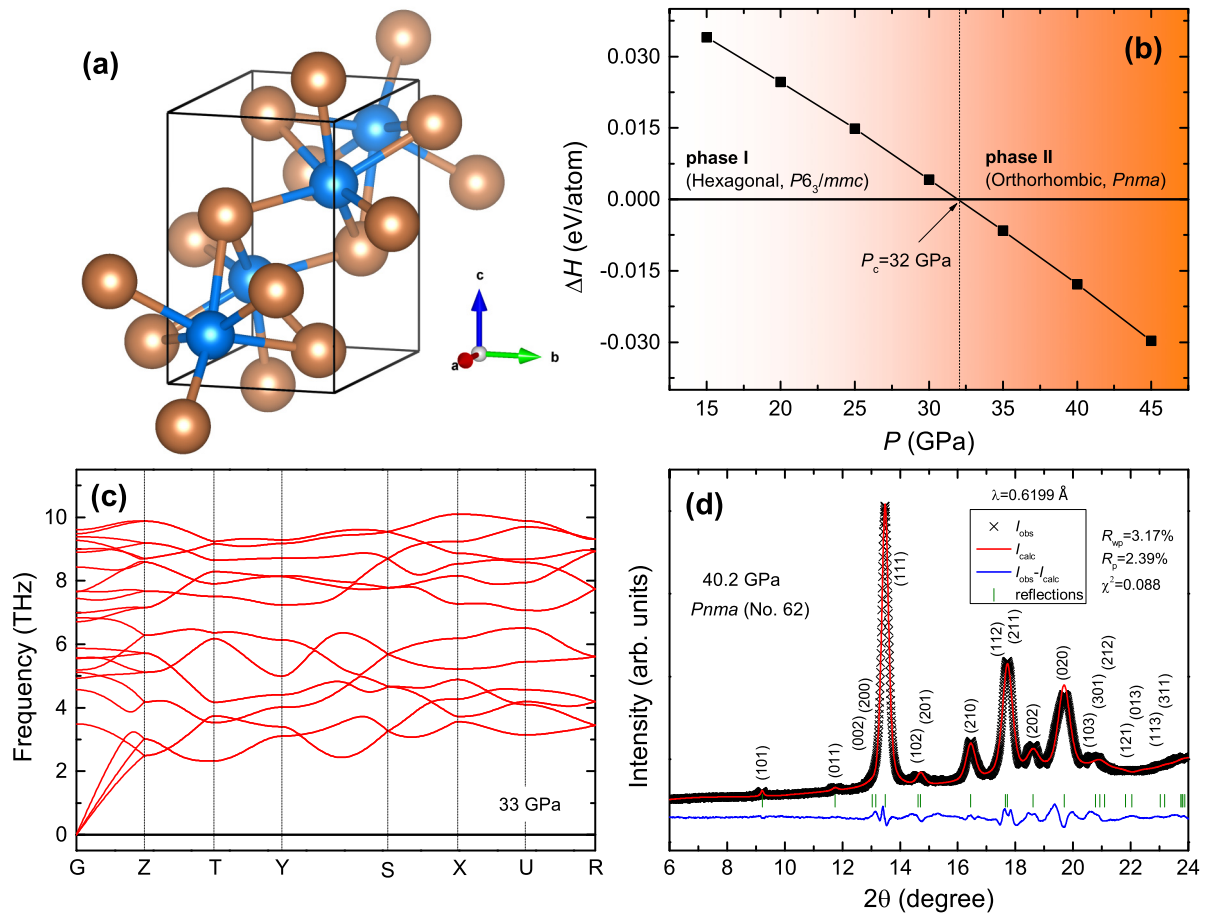


FIG. 8. (a) Theoretically predicted crystal structure of CoSb. (b) Enthalpy difference as a function of pressure between the hexagonal and orthorhombic phases. (c) Phonon dispersion for the high-pressure *Pnma* phase at 33 GPa. No imaginary frequency appears for both acoustic and optical branches near the Brillouin zone center (*G* point) and other high-symmetry points. (d) Rietveld refinement of CoSb at 40.2 GPa.

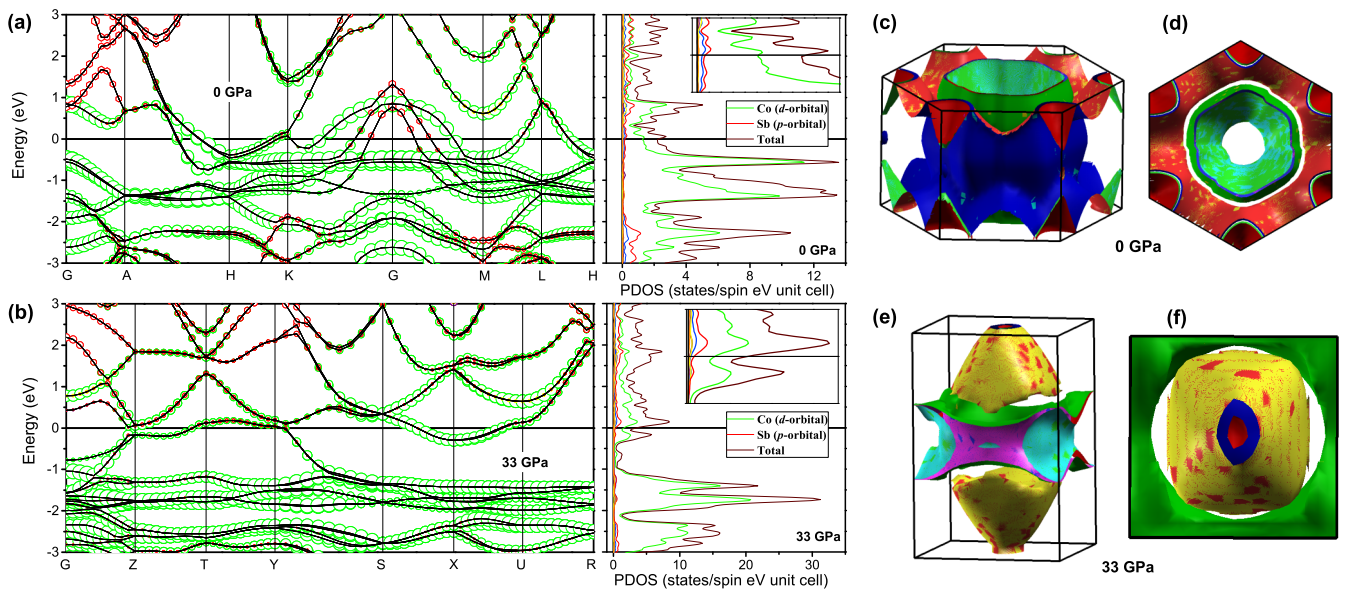


FIG. 9. Electronic band structure with spin-orbit coupling (SOC) for (a) ambient hexagonal *P6₃/mmc* phase, and (b) high-pressure orthorhombic *Pnma* phase at 33 GPa. Purple line: *s* orbital of Co, blue line: *p* orbital of Co, yellow line: *s* orbital of Sb, orange line: *d* orbital of Sb. (c) and (d) Fermi surface of the ambient hexagonal phase. (e) and (f) Fermi surface of the high-pressure orthorhombic phase.

measurements on layered TiSe_2 [63,64], the pressure-tuned variation of $\rho \approx T^{n'}$ at low temperature was observed. Simultaneously, the occurrence of low- T_c superconductivity coincidentally accompanies a noticeable decrease of the exponent from a high value ($n' \approx 3$) to a lower one. Although a small dip in $n'(P)$ appears for CoSb crossing the SPT, as shown in the inset of Fig. 2(b), it is a pity that no superconductivity is detected down to 2 K. In some A-15 superconductors such as V_3Si [42], the increase of the disorders by neutron irradiation causes a significant decrease of T_c ; meanwhile, the n' value grows from ~ 2 for pristine to 4.6 for heavily irradiated samples. For the well-studied topological insulator Bi_2Se_3 , the $n' = 3.38$ was obtained at low temperature, and no superconductivity was detected down to 0.14 K (see Figs. S5 and S6 in the Supplemental Material [38]), but a smaller value of $n' = 2.58$ for the superconducting $\text{Cu}_{0.09}\text{Bi}_2\text{Se}_3$ ($T_c = 4.18$ K) is reported [65]. Compared with pressurized CoSb , a similar situation occurs in TaAs_2 [41]. It also shows a robust $\rho \approx T^3$ at low temperature, yet no superconductivity was detected at 2 K up to 36.6 GPa. These experimental facts highlight the crucial role of the low-temperature $\rho \approx T^2$ part associated with the EEI in inducing or enhancing superconductivity.

In unconventional high- T_c superconductors, the strong electron correlations are thought to be relevant for the non-Fermi liquid behavior [66–68], in which the $\rho \approx T^{n'}$ with $1 \leq n' \leq 2$ obeys and the maximum T_c value is reached at $n' \cong 1$. When crossing the overdoped region, the T_c gradually decreases and eventually disappears, accompanying an increase of the exponent n' up to two, accessing the Fermi liquid region. Importantly, it is shown that the strength of the electron correlation is connected to optimize the T_c value in iron-based superconductors [56]. In this context, the EEI is also an indispensable factor in high- T_c superconductors, although the pairing mechanism is presumed to be different from the conventional phonon-mediated superconductors.

Since the EPI enhanced by the interface is likely to be the main factor for enhancing the T_c in monolayer FeSe [69] or monolayer CoSb [9] on the SrTiO_3 substrate, we tentatively discuss the absence of superconductivity in pressurized bulk CoSb within the electron-phonon coupling scenario. According to Bardeen-Cooper-Schrieffer (BCS) theory [62,70], the T_c is given by $T_c = 1.14\Theta_D \exp[-1/N(E_F)V_0]$ in a weak coupling limit with $N(E_F)V_0 = \lambda - \mu^*$, where V_0 is an effective EEI potential containing an attractive part from EPI and a repulsive electron-electron contribution. If $V_0 \rightarrow 0$ or the λ value is close to μ^* , then superconductivity will not be expected. This limit is presumably at play in pressurized CoSb . In detail, it can be inferred from the $\rho(T)$ for pressurized CoSb that there is a negligible contribution of the electron-electron scattering to the conduction at low temperature. Only the robust and strong electron-phonon scattering is involved down to 2 K. It seems that the absence of substantial contribution from the $\rho \approx T^{n'}$ ($1 \leq n' \leq 2$) part correlates with the undetectable superconductivity down to 2 K for CoSb under pressure. As the n' value increases, the T_c tends to decrease for low- T_c superconductors, unconventional high- T_c cuprates, and iron-based superconductors, as plotted in Fig. S5 in the Supplemental Material [38] (see also Refs. [41,42,63–68,71–93] therein). This supports that the electronic correlation is a fundamental factor for optimizing superconductivity.

According to a recent theoretical study of the resistivity saturation in A-15 superconducting compounds [55], the resistivity saturation temperature can be pushed to higher values as the onsite Coulomb repulsion U increases. This means that stronger electron correlations would destroy resistivity saturation. In the case of CoSb , the resistivity saturation becomes more prominent with loading pressure and could survive at high pressures up to 42.0 GPa. Together with the dominant $\rho \approx T^3$ at low temperature, our results indicate that the pressure fails to enhance the strength of the electron correlation in CoSb . Thus, the superconducting transition is unfavorable under pressure.

IV. SUMMARY

To explore the possible pressure-induced superconductivity in NiAs-type CoSb associated with lattice instability, we investigated the evolution of the electrical and structural properties of the bulk sample under pressure. First, a pressure-induced structure phase transition from hexagonal to orthorhombic emerged between 11.7 and 16.2 GPa, but there is no concomitant superconducting transition down to 2 K with the applied pressure up to 42.0 GPa. Second, an abnormal increase of resistivity with increasing pressure was observed at ~ 13.4 GPa. Also, a more and more prominent resistivity saturation feature appeared at high temperature with increasing pressure. The Hall effect analysis supports that an electronic transition featured by a semimetal-semimetal transition and a n - p switch occurred at ~ 10 GPa due to the SPT. Interestingly, the orthorhombic phase hosts the temperature-driven p - n switch at ~ 90 K as well. This demonstrates that the CNP can be realized by either pressure or temperature for semimetal CoSb . The temperature-dependent resistivity was analyzed in a parallel-resistor model framework to understand the superconductivity absence in bulk CoSb . The resistivity vs temperature shows robust $\rho(T) \approx T^3$ behavior < 30 K for the two phases, implying a negligible electron-electron scattering. This may be one key ingredient causing an unfavorable superconducting transition in bulk CoSb . The parallel-resistor model, including the s - d interband scattering, can describe the $\rho(T)$ curves well, indicating that the s - d interband scattering dominates the conductivity of both hexagonal and orthorhombic CoSb under pressure. We hope our results trigger further attention to investigate the underlying physics linking the absence or weakening of superconductivity and the robust $\rho \approx T^3$ relation at low temperature in the involved materials.

ACKNOWLEDGMENTS

We thank Xueyan Du for her technical support. We also thank Zhenhai Yu and Lili Zhang for their assistance on setting up the synchrotron XRD experiment at BL15U1, SSRF, Shanghai, China. This paper is supported by the National Natural Science Foundation of China (Grants No. 11804011, No. 11974112, No. U1930401, No. 51527801, and No. 12074153). Y.F. is sponsored by Shanghai Sailing Program No. 20YF1455100.

- [1] A. Kjekshus, K. P. Walseth, S. E. Rasmussen, D. Heinegård, A. T. Balaban, and J. C. Craig, *Acta Chem. Scand.* **23**, 2621 (1969).
- [2] G. Hanninger, H. Ipsier, P. Terzieff, and K. L. Komarek, *J. Less Common Met.* **166**, 103 (1990).
- [3] P. Terzieff and H. Ipsier, *Monatsh. Chem.* **123**, 35 (1992).
- [4] P. Amornpitoksuk, D. Ravot, A. Mauger, and J. C. Tedenac, *Phys. Rev. B* **77**, 144405 (2008).
- [5] C. Xian, Y. Wang, J. Wang, L. Zhang, Y. Han, L. Cao, and Y. Xiong, *J. Supercond. Novel Magn.* **31**, 1841 (2018).
- [6] W. B. Pearson, *Can. J. Phys.* **35**, 886 (1957).
- [7] G. Rogl and P. Rogl, *Mater. Today Phys.* **3**, 48 (2017).
- [8] Y. Tang, Z. M. Gibbs, L. A. Agapito, G. Li, H.-S. Kim, M. B. Nardelli, S. Curtarolo, and G. J. Snyder, *Nat. Mater.* **14**, 1223 (2015).
- [9] W. Ding, J. Zeng, W. Qin, P. Cui, and Z. Zhang, *Phys. Rev. Lett.* **124**, 027002 (2020).
- [10] B. T. Matthias and J. K. Hulm, *Phys. Rev.* **89**, 439 (1953).
- [11] N. T. Huy, A. Gasparini, D. E. de Nijs, Y. Huang, J. C. P. Klaasse, T. Gortenmulder, A. de Visser, A. Hamann, T. Görlach, and H. v. Löhneysen, *Phys. Rev. Lett.* **99**, 067006 (2007).
- [12] C. Petrovic, P. G. Pagliuso, M. F. Hundley, R. Movshovich, J. L. Sarrao, J. D. Thompson, Z. Fisk, and P. Monthoux, *J. Phys. Condens. Matter* **13**, L337 (2001).
- [13] K. Takada, H. Sakurai, E. Takayama-Muromachi, F. Izumi, R. A. Dilanian, and T. Sasaki, *Nature* **422**, 53 (2003).
- [14] H. Mizoguchi, T. Kuroda, T. Kamiya, and H. Hosono, *Phys. Rev. Lett.* **106**, 237001 (2011).
- [15] J. Hu, C. Le, and X. Wu, *Phys. Rev. X* **5**, 041012 (2015).
- [16] Q.-Y. Wang, Z. Li, W.-H. Zhang, Z.-C. Zhang, J.-S. Zhang, W. Li, H. Ding, Y.-B. Ou, P. Deng, K. Chang, J. Wen, C.-L. Song, K. He, J.-F. Jia, S.-H. Ji, Y.-Y. Wang, L.-L. Wang, X. Chen, X.-C. Ma, and Q.-K. Xue, *Chin. Phys. Lett.* **29**, 037402 (2012).
- [17] C. Ding, G. Gong, Y. Liu, F. Zheng, Z. Zhang, H. Yang, Z. Li, Y. Xing, J. Ge, K. He, W. Li, P. Zhang, J. Wang, L. Wang, and Q.-K. Xue, *ACS Nano* **13**, 10434 (2019).
- [18] L. P. Gor'kov and V. Z. Kresin, *Rev. Mod. Phys.* **90**, 011001 (2018).
- [19] H.-K. Mao, X.-J. Chen, Y. Ding, B. Li, and L. Wang, *Rev. Mod. Phys.* **90**, 015007 (2018).
- [20] K. Kirshenbaum, P. S. Syers, A. P. Hope, N. P. Butch, J. R. Jeffries, S. T. Weir, J. J. Hamlin, M. B. Maple, Y. K. Vohra, and J. Paglione, *Phys. Rev. Lett.* **111**, 087001 (2013).
- [21] M. Li, K. Xu, M. Xu, Y. Fang, Z. Yan, N. Li, Z. Yu, J. Zhang, C. Kenney-Benson, X. Wang, and L. Wang, *Phys. Rev. B* **100**, 224521 (2019).
- [22] Y. Zhou, P. Lu, Y. Du, X. Zhu, G. Zhang, R. Zhang, D. Shao, X. Chen, X. Wang, M. Tian, J. Sun, X. Wan, Z. Yang, W. Yang, Y. Zhang, and D. Xing, *Phys. Rev. Lett.* **117**, 146402 (2016).
- [23] T. Liang, S. Kushwaha, J. Kim, Q. Gibson, J. Lin, N. Kioussis, R. J. Cava, and N. P. Ong, *Sci. Adv.* **3**, e1602510 (2017).
- [24] T. Nishimura, H. Sakai, H. Mori, K. Akiba, H. Usui, M. Ochi, K. Kuroki, A. Miyake, M. Tokunaga, Y. Uwatoko, K. Katayama, H. Murakawa, and N. Hanasaki, *Phys. Rev. Lett.* **122**, 226601 (2019).
- [25] L. J. v. d. Pauw, *Philips Res. Rep.* **13**, 1 (1958).
- [26] C. Prescher and V. B. Prakapenka, *High Pressure Res.* **35**, 223 (2015).
- [27] A. C. Larson and R. B. Von Dreele, *General Structure Analysis System (GSAS)*, Los Alamos National Laboratory Report No. LAUR 86-748 (The Regents of the University of California, Los Alamos, 2004).
- [28] B. Toby, *J. Appl. Crystallogr.* **34**, 210 (2001).
- [29] H. K. Mao, J. Xu, and P. M. Bell, *J. Geophys. Res. Solid Earth* **91**, 4673 (1986).
- [30] J. Hafner, *Comput. Phys. Commun.* **177**, 6 (2007).
- [31] G. Kresse and J. Furthmüller, *Phys. Rev. B* **54**, 11169 (1996).
- [32] A. O. Lyakhov, A. R. Oganov, H. T. Stokes, and Q. Zhu, *Comput. Phys. Commun.* **184**, 1172 (2013).
- [33] C. W. Glass, A. R. Oganov, and N. Hansen, *Comput. Phys. Commun.* **175**, 713 (2006).
- [34] J. P. Perdew, K. Burke, and M. Ernzerhof, *Phys. Rev. Lett.* **77**, 3865 (1996).
- [35] N. A. W. Holzwarth, A. R. Tackett, and G. E. Matthews, *Comput. Phys. Commun.* **135**, 329 (2001).
- [36] K. Parlinski, Z. Q. Li, and Y. Kawazoe, *Phys. Rev. Lett.* **78**, 4063 (1997).
- [37] T. Chen, J. C. Mikkelsen, and G. B. Charlan, *J. Cryst. Growth* **43**, 5 (1978).
- [38] See Supplemental Material at <http://link.aps.org/supplemental/10.1103/PhysRevB.104.054511> for more details on the Rietveld refinement profiles and tabulated results, Hall data, T_c versus n' relation for selected materials and resistivity at ultralow temperature for single crystal Bi_2Se_3 .
- [39] F. Birch, *Phys. Rev.* **71**, 809 (1947).
- [40] A. H. Wilson, *Proc. R. Soc. A* **167**, 580 (1938).
- [41] H. Wang, C. Pei, H. Su, Z. Yu, M. Li, W. Xia, X. Liu, Q. Liang, J. Zhao, C. Zhou, N. Yu, X. Wang, Z. Zou, L. Wang, Y. Qi, and Y. Guo, *Appl. Phys. Lett.* **115**, 122403 (2019).
- [42] R. Caton and R. Viswanathan, *Phys. Rev. B* **25**, 179 (1982).
- [43] Z. Fisk and G. W. Webb, *Phys. Rev. Lett.* **36**, 1084 (1976).
- [44] N. Morton, B. W. James, and G. H. Wostenholm, *Cryogenics* **18**, 131 (1978).
- [45] O. Gunnarsson, M. Calandra, and J. E. Han, *Rev. Mod. Phys.* **75**, 1085 (2003).
- [46] N. E. Hussey, K. Takenaka, and H. Takagi, *Philos. Mag.* **84**, 2847 (2004).
- [47] E. Grüneisen, *Ann. Phys. Lpz.* **408**, 530 (1933).
- [48] J. M. Ziman, in *Electrons and Phonons: The Theory of Transport Phenomena in Solids* (Oxford University Press, Oxford, 1960), p. 369.
- [49] D. B. Poker and C. E. Klabunde, *Phys. Rev. B* **26**, 7012 (1982).
- [50] H. Wiesmann, M. Gurvitch, H. Lutz, A. Ghosh, B. Schwarz, M. Strongin, P. B. Allen, and J. W. Halley, *Phys. Rev. Lett.* **38**, 782 (1977).
- [51] M. Gurvitch, *Phys. Rev. B* **24**, 7404 (1981).
- [52] G. K. White and R. J. Tainsh, *Phys. Rev. Lett.* **19**, 165 (1967).
- [53] J. Bardeen, *J. Appl. Phys.* **11**, 88 (1940).
- [54] M. Gurvitch and A. T. Fiory, *Phys. Rev. Lett.* **59**, 1337 (1987).
- [55] E. Perepelitsky and B. S. Shastry, *Phys. Rev. Lett.* **122**, 026602 (2019).
- [56] Z. R. Ye, Y. Zhang, F. Chen, M. Xu, J. Jiang, X. H. Niu, C. H. P. Wen, L. Y. Xing, X. C. Wang, C. Q. Jin, B. P. Xie, and D. L. Feng, *Phys. Rev. X* **4**, 031041 (2014).
- [57] S. Zeng, C. S. Tang, X. Yin, C. Li, M. Li, Z. Huang, J. Hu, W. Liu, G. J. Omar, H. Jani, Z. S. Lim, K. Han, D. Wan, P. Yang, S. J. Pennycook, A. T. S. Wee, and A. Ariando, *Phys. Rev. Lett.* **125**, 147003 (2020).
- [58] N. F. Mott, in *Metal Insulator Transitions* (Taylor and Francis, London, 1990).

- [59] J. Garai, [arXiv:physics/0703001](https://arxiv.org/abs/physics/0703001).
- [60] T. Zhang, Y. Jiang, Z. Song, H. Huang, Y. He, Z. Fang, H. Weng, and C. Fang, *Nature* **566**, 475 (2019).
- [61] M. Qi, C. An, Y. Zhou, H. Wu, B. Zhang, C. Chen, Y. Yuan, S. Wang, Y. Zhou, X. Chen, R. Zhang, and Z. Yang, *Phys. Rev. B* **101**, 115124 (2020).
- [62] J. Bardeen, L. N. Cooper, and J. R. Schrieffer, *Phys. Rev.* **108**, 1175 (1957).
- [63] A. F. Kusmartseva, B. Sipos, H. Berger, L. Forró, and E. Tutiš, *Phys. Rev. Lett.* **103**, 236401 (2009).
- [64] B. Wang, Y. Liu, K. Ishigaki, K. Matsubayashi, J. Cheng, W. Lu, Y. Sun, and Y. Uwatoko, *Phys. Rev. B* **95**, 220501(R) (2017).
- [65] Y. Fang, W.-L. You, and M. Li, *New J. Phys.* **22**, 053026 (2020).
- [66] H. Takagi, B. Batlogg, H. L. Kao, J. Kwo, R. J. Cava, J. J. Krajewski, and W. F. Peck, *Phys. Rev. Lett.* **69**, 2975 (1992).
- [67] R. A. Cooper, Y. Wang, B. Vignolle, O. J. Lipscombe, S. M. Hayden, Y. Tanabe, T. Adachi, Y. Koike, M. Nohara, H. Takagi, C. Proust, and N. E. Hussey, *Science* **323**, 603 (2009).
- [68] S. Kasahara, T. Shibauchi, K. Hashimoto, K. Ikada, S. Tonegawa, R. Okazaki, H. Shishido, H. Ikeda, H. Takeya, K. Hirata, T. Terashima, and Y. Matsuda, *Phys. Rev. B* **81**, 184519 (2010).
- [69] J. J. Lee, F. T. Schmitt, R. G. Moore, S. Johnston, Y. T. Cui, W. Li, M. Yi, Z. K. Liu, M. Hashimoto, Y. Zhang, D. H. Lu, T. P. Devereaux, D. H. Lee, and Z. X. Shen, *Nature* **515**, 245 (2014).
- [70] G. Grimvall, *Phys. Scr.* **14**, 63 (1976).
- [71] C. Proust, B. Vignolle, J. Levallois, S. Adachi, and N. E. Hussey, *Proc. Natl Acad. Sci. USA* **113**, 13654 (2016).
- [72] T. Ito, K. Takenaka, and S. Uchida, *Phys. Rev. Lett.* **70**, 3995 (1993).
- [73] S. Nakamae, K. Behnia, N. Mangkorntong, M. Nohara, H. Takagi, S. J. C. Yates, and N. E. Hussey, *Phys. Rev. B* **68**, 100502 (2003).
- [74] R. L. Greene, P. R. Mandal, N. R. Poniatowski, and T. Sarkar, *Annu. Rev. Condens. Matter Phys.* **11**, 213 (2020).
- [75] Y. Ando and T. Murayama, *Phys. Rev. B* **60**, R6991 (1999).
- [76] J. P. Sun, P. Shahi, H. X. Zhou, Y. L. Huang, K. Y. Chen, B. S. Wang, S. L. Ni, N. N. Li, K. Zhang, W. G. Yang, Y. Uwatoko, G. Xing, J. Sun, D. J. Singh, K. Jin, F. Zhou, G. M. Zhang, X. L. Dong, Z. X. Zhao, and J. G. Cheng, *Nat. Commun.* **9**, 380 (2018).
- [77] X. Xing, Y. Sun, X. Yi, M. Li, J. Feng, Y. Meng, Y. Zhang, W. Li, N. Zhou, X. He, J.-Y. Ge, W. Zhou, T. Tamegai, and Z. Shi, *Supercond. Sci. Technol.* **34**, 055006 (2021).
- [78] M. Gooch, B. Lv, B. Lorenz, A. M. Guloy, and C.-W. Chu, *Phys. Rev. B* **79**, 104504 (2009).
- [79] X. F. Wang, T. Wu, G. Wu, R. H. Liu, H. Chen, Y. L. Xie, and X. H. Chen, *New J. Phys.* **11**, 045003 (2009).
- [80] N. Maksimovic, I. M. Hayes, V. Nagarajan, J. G. Analytis, A. E. Koshelev, J. Singleton, Y. Lee, and T. Schenkel, *Phys. Rev. X* **10**, 041062 (2020).
- [81] R. H. Liu, G. Wu, T. Wu, D. F. Fang, H. Chen, S. Y. Li, K. Liu, Y. L. Xie, X. F. Wang, R. L. Yang, L. Ding, C. He, D. L. Feng, and X. H. Chen, *Phys. Rev. Lett.* **101**, 087001 (2008).
- [82] Y. Maeno, K. Yoshida, H. Hashimoto, S. Nishizaki, S.-i. Ikeda, M. Nohara, T. Fujita, A. P. Mackenzie, N. E. Hussey, J. G. Bednorz, and F. Lichtenberg, *J. Phys. Soc. Japan* **66**, 1405 (1997).
- [83] N. E. Hussey, A. P. Mackenzie, J. R. Cooper, Y. Maeno, S. Nishizaki, and T. Fujita, *Phys. Rev. B* **57**, 5505 (1998).
- [84] Y. Zhou, C. Chen, Y. Zhou, X. Chen, C. Gu, C. An, B. Zhang, Y. Yuan, H. Wu, R. Zhang, L. Zhang, X. Zhu, X. Yang, and Z. Yang, *Phys. Rev. B* **99**, 125104 (2019).
- [85] K. Zhou, J. Deng, L. Guo, and J. Guo, *Chin. Phys. Lett.* **37**, 097402 (2020).
- [86] X.-M. Zhao, K. Zhang, Z.-Y. Cao, Z.-W. Zhao, V. V. Struzhkin, A. F. Goncharov, H.-K. Wang, A. G. Gavriliuk, H.-K. Mao, and X.-J. Chen, *Phys. Rev. B* **101**, 134506 (2020).
- [87] Y. S. Eo, S. R. Saha, H. Kim, S. Ran, J. A. Horn, H. Hodovanets, J. Collini, W. T. Fuhrman, A. H. Nevidomskyy, N. P. Butch, M. S. Fuhrer, and J. Paglione, [arXiv:2101.03102](https://arxiv.org/abs/2101.03102).
- [88] Y. Mizukami, M. Kończykowski, O. Tanaka, J. Juraszek, Z. Henkie, T. Cichorek, and T. Shibauchi, *Phys. Rev. Res.* **2**, 043428 (2020).
- [89] B. R. Ortiz, L. C. Gomes, J. R. Morey, M. Winiarski, M. Bordelon, J. S. Mangum, I. W. H. Oswald, J. A. Rodriguez-Rivera, J. R. Neilson, S. D. Wilson, E. Ertekin, T. M. McQueen, and E. S. Toberer, *Phys. Rev. Mater.* **3**, 094407 (2019).
- [90] B. R. Ortiz, P. M. Sarte, E. M. Kenney, M. J. Graf, S. M. L. Teicher, R. Seshadri, and S. D. Wilson, *Phys. Rev. Mater.* **5**, 034801 (2021).
- [91] S. Sun, Q. Wang, P.-J. Guo, K. Liu, and H. Lei, *New J. Phys.* **18**, 082002 (2016).
- [92] F. F. Tafti, Q. D. Gibson, S. K. Kushwaha, N. Haldolaarachchige, and R. J. Cava, *Nat. Phys.* **12**, 272 (2016).
- [93] H. Gu, F. Tang, Y. R. Ruan, J. M. Zhang, R. J. Tang, W. Zhao, R. Zhao, L. Zhang, Z. D. Han, B. Qian, X. F. Jiang, and Y. Fang, *Phys. Rev. Mater.* **4**, 124204 (2020).